Spectral Hardening in Large Solar Flares

P. C. Grigis and A. O. Benz

Institute of Astronomy, ETH Zurich, 8092 Zurich, Switzerland

ABSTRACT

Context. Bremsstrahlung hard X-rays emitted by electrons accelerated in solar flares are an important diagnostic for understanding the acceleration mechanism. Strong spectral variability is observed, usually following a soft-hard-soft pattern during impulsive emission spikes. In addition to this behavior, larger events occasionally show gradual hardening, usually in the late phase of the flares.

Aims. We study quantitatively the hard X-ray spectral evolution of large solar flares featuring hardening trends. In particular, we investigate whether two different acceleration mechanisms are responsible for the impulsive and gradual phases.

Methods. Spectral fitting of the non-thermal emission at high (~ 4 s) and medium (~ 32 s) cadence are obtained from RHESSI data, yielding time profiles of the non-thermal fit parameters (flux, spectral index, spectral curvature) for five X-class solar flares. The temporal evolution of the spectra is compared with the configuration and motion of the hard X-ray sources in RHESSI images.

Results. Both soft-hard-soft (impulsive) phases and hardening (gradual) phases are observed during the events and are well described by piecewise linear dependence of the spectral index on the logarithm of the flux. The transition between the impulsive and gradual phases is smooth and progressive rather than abrupt, both in spectra and images. Comparison with a pure trapping model in the late phase leads to good agreement with the observation for the spectral index vs. flux relation, but poor predictions for the spectral curvature.

Conclusions. The evidence we find points toward a single acceleration mechanism acting in the two phases, rather than two different separated mechanisms, because the impulsive and gradual phases are closely interconnected in time and space.

Key words. Sun: flares – Sun: X-rays, gamma rays – Acceleration of particles

1. Introduction

Large solar flares are very bright hard X-ray sources. This emission originates from energetic electrons with energies mainly in the 10s and 100s of keV, believed to be accelerated in the corona. These electrons have a short lifetime in regions dense enough to generate substantial hard X-ray emission, and therefore react quickly to changes in the acceleration, transport and emission processes. While it may be hard do disentangle the contribution of the different effects, the study of the temporal evolution of the hard X-ray spectra is a valuable tool to probe these processes. Flare models and theories should be able to account for the behavior of the observed hard X-ray spectra as they change during an event.

Observations of the spectral hard X-ray evolution have discovered two main trends: a soft-hard-soft (SHS) spectral evolution of emission peaks, and a progressive hardening during whole events (SHH, soft-hard-harder).

The SHS behavior of emission spikes was discovered by Parks & Winckler (1969), and since then has been reported by many others. More recently, Grigis & Benz (2004) surveyed quantitatively the spectral evolution of emission spikes during M class events, finding that nearly all rise and decay phases

of the peaks show the SHS behavior. The excursion in both flux and hardness can be very different from peak to peak, but consistently shows a characteristic property: the spectral index can be described by a linear function of the logarithm of the flux measured at a fixed energy (Grigis & Benz 2005a). The SHS pattern has also been observed in looptop sources (Battaglia & Benz 2006), and thus it is likely to be a characteristic signature of the acceleration rather than the propagation process. Detailed modeling of transit-time damping acceleration of electrons show that SHS behavior can be reproduced when the effects of particle trapping and escape are taken in account (Grigis & Benz 2006).

The SHH behavior was first observed by Frost & Dennis (1971), where in the later phase of the event the spectral index stayed constant at a harder value than measured during the first, impulsive, SHS peak. Further studies were done by Cliver et al. (1986) and Kiplinger (1995) using data from the Hard X-Ray Burst Spectrometer (HXRBS) on SMM. The distinctive feature of the SHH evolution is the absence of softening as the flux decreases.

Kiplinger found two different subtypes of behavior:

- hardening during a particular peak.
- hardening during the decay of the whole event.

In the first subtype, the hardening is limited to a short period during the flare, and after the emission peak the flux may soften again. Events of the second subtype (corresponding to the classic flare with a gradual phase) typically have some SHS peaks at the beginning but progressively harden afterwards. Despite the name, the hardening can already start before the largest peak and therefore is not necessarily limited to the decay phase. Kiplinger reported a high association of the presence of hardening phases with the occurrence of energetic interplanetary proton events.

We note here that the two classes of spectral evolution (SHS and SHH) are by no means separated: most SHH events show impulsive SHS peaks at the beginning. The two different kinds of spectral evolution seem to support the view that there are two different stages in the events: an impulsive phase at the beginning followed by a gradual component, with different acceleration mechanisms during these phases. This scenario was first proposed to explain radio observations (Wild et al. 1963), where the first (impulsive) phase was thought to accelerate the fast electrons producing gyrosynchroton emission, and the second (gradual) phase was linked to traveling shocks (type II radio bursts) accelerating electrons and ions. This idea was then used to explain hard X-ray observations (Frost & Dennis 1971). Later, these shocks were linked with Coronal Mass Ejections (CMEs). Occulted flares seemed to confirm this scenario (Hudson et al. 1982). This interpretation however could not explain the position of the dominant hard X-ray source seen during the gradual phase: imaging observations by Hinotori (Ohki et al. 1983) showed that the hard X-ray emission comes from too low in the solar corona to justify the connection with type II radio bursts. Kahler (1984) argued that the impulsive phase is followed by two independent acceleration processes, the first happening in the post-flare loop arcade and responsible for the late-phase hard X-ray emitting electrons, and the second higher up in the corona, shock driven, accelerating interplanetary electrons and ions. This was later corroborated by Cliver et al. (1986) using SMM observations.

Stochastic acceleration can reproduce the observed SHS behavior (at least in simple one dimensional settings) when particle trapping is taken into account (Grigis & Benz 2006), but the model cannot at the same time describe hardening when the flux decays. If both the SHS and SHH phases of electron acceleration happens in the same events, why are their spectral behavior so different? Do they really represent different acceleration mechanisms? To find an observational answer to these questions, we need simultaneous imaging and spectral data analysis for large flares, a task well suited for the Reuven Ramaty High Energy Solar Spectrometric Imager (RHESSI; Lin et al. 2002).

In this paper, we analyze RHESSI hard X-ray data and describe in a quantitative way the spectral evolution of large solar flares in the non-thermal energy range. We test the hypothesis claiming that two different electron acceleration mechanisms are acting during large solar flares. To this end we also compare the spectral evolution with the configuration and motion of the non-thermal footpoint sources.

Table 1. Chronological list of the selected events.

Date	GOES peak		Panel in
	time	flux	Figs. 2 and 3
7-NOV-2004	16:05	X2.0	F
10-NOV-2004	02:13	X2.6	A
17-JAN-2005	09:52	X3.9	B
19-JAN-2005	08:23	X1.4	C & D
20-JAN-2005	07:01	X7.1	E

2. Method

The goal of this paper is a detailed quantitative study of the spectral evolution of solar flares showing a hardening trend in RHESSI observations. Rather than attempting a comprehensive statistical study of a large number of flares, the analysis is restricted to a few events, studied in more detail. Therefore, we do not estimate the frequency of occurrence of hardening in all flares. This has been done by Kiplinger (1995) using SMM/HXRBS data, who reports 24 occurrences of this behavior out of 152 events with peak flux count rate larger than 5000 counts s^{-1}. Most of the hardening events reported by Kiplinger are in the upper M and X GOES class. This implies that flares with hardening are likely to be large. From his kind of observations alone it is however unclear whether this is a real effect, or an observational bias due to the weak hard component lying below the observational threshold in smaller flares.

We selected flares with a GOES flux above X1 during the RHESSI observation time windows. 50 events satisfying this condition were found in the period from the start of the mission (February 2002) to September 2006. We additionally required that the rise, main and decay phases were well observed, to study the spectral evolution in time. This left us with 12 candidates.

As a first approximation, the presence of hardening behavior can be established by studying the count rates in the energy range from 30 to 60 keV. We fitted the spectral index separately in in three energy bands (30–40 keV, 40–50 keV, 50–60 keV) and looked for either trends of progressive hardening or the presence of a late hard phase. The lower band is sometimes contaminated by thermal emission, but this can be easily spotted by comparing it with the other bands. While this method uses the count rates and is not sufficient for the quantitative study of the spectral behavior, we found it adequate for the simpler task of identifying candidate events for spectral hardening. Although it may have missed some events where hardening happens in a phase of low flux and where it may be confused with the background. After discarding two further events with high pileup, we found 5 well-observed events with a clear signature of hardening. These are listed in Table 1.

For each of the selected events, the instrumental response matrices and count-rate spectrograms covering the energy range from 3 to 500 keV were generated for the front segments with a temporal resolution of one RHESSI spin period (approximatively 4 s). The spatially integrated spectra were fitted in the range 12 to 500 keV to a photon model with two components: an isothermal component at low energies (below about 20-40 keV) and a nonthermal component at higher energies.
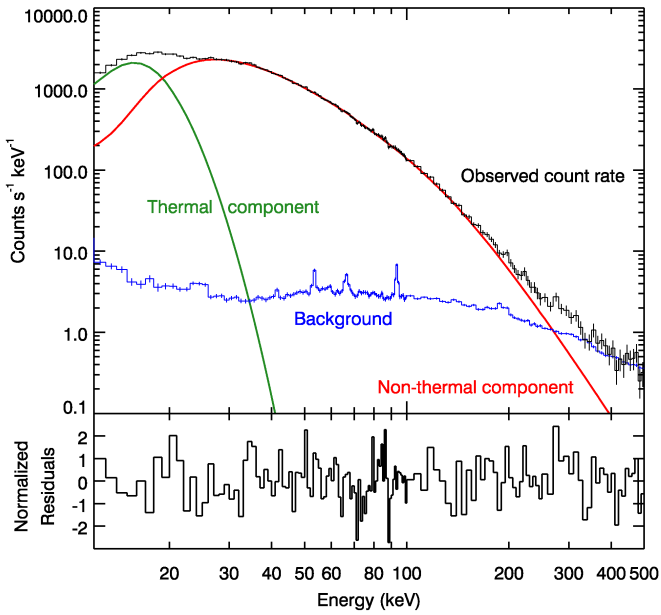
Fig. 1. Observed count spectrum with the best fit model components. The spectrum was integrated for 4 seconds around 17-JAN-2005 09:43:36 UT. The thermal and non-thermal (log-parabolic) component, as well as the background are shown. For clarity, the total model consisting of the sum of the three components is not shown directly on the observed count spectra, but its normalized residuals are shown below instead. The reduced χ^2 for this spectrum equals 0.94.

The non-thermal X-ray component is usually fitted with a power-law function of the energy, having 2 free parameters. However, sometimes it is observed that the spectrum tends to steepen at higher energies. In the literature this is usually accounted for by using a broken power-law model (e.g. Dulk et al. 1992, Battaglia et al. 2005). There are some disadvantages in the broken power-law model: a) it is not physical, in the sense that any continuous electron distribution emitting X-rays should generate a differentiable photon spectrum, and b) the location of the break point is poorly determined by the observations.

We argue that there is a simple extension to the power-law model which both turns down at higher energies and is smooth. Recalling that a power-law function plotted in log-log space is a straight line, we choose as a "natural" extension to the next order a parabolic model in log-log space, described by the function

$$F(E) = F_{E_0} \cdot \left(\frac{E}{E_0}\right)^{\gamma - \eta \log (E/E_0)}, \qquad (1)$$

The 3 model parameters are the spectral index $\gamma < 0$, the parabolic coefficient η, which we will refer to as the *spectral curvature* although, strictly speaking, the geometric curvature of the parabola is not constant, but equals -2η in the vertex and vanishes at infinity. The normalization is provided by the parameter F_{E_0}, amounting to the flux at the (fixed) normalization energy E_0.

In the special case $\eta = 0$, the (unbroken) power-law model is recovered. We note here that a log-parabolic model has been used to describe observed X-ray spectra of pulsars (Massaro et al. 2000).

In summary, the reasons for preferring the log-parabolic model over the more usual broken power-law are:

1. It is simpler then the broken power-law, as it allows only 3 instead of 4 free parameters.
2. For the vast majority of the time intervals, it produces similar values of χ^2 as the broken-power law.
3. It is differentiable, therefore there exists a continuous electron spectrum producing the photon spectrum. This is not the case for the broken power-law, where a discontinuity is needed in the electron spectrum, which may quickly be eliminated by kinetic plasma processes. The spectral index increases linearly with $\log E$.
4. It allows a better comparison with acceleration models which naturally produce slightly curved electron spectra (like stochastic acceleration).

We fit the spectra to a photon model with an isothermal component at lower energies and a log-parabolic component as given above at higher energies. The background is taken into account in the following way: the pre-event and post-event background spectra are measured and averaged (in some cases, particle contamination prevented to obtain both of them, and only one was taken instead), yielding a reference background spectrum.

During the fitting process, the model photon spectrum is folded with the response matrix, yielding the expected count spectrum from the model. The reference background spectrum is then multiplied with a normalization factor λ and added to the model counts, where λ is an additional fit parameter for the model fitting and is constrained between 0.5 and 2. This correspond approximatively to the maximum excursion in RHESSI's background in the front segments during an orbit. The parameter η is constrained to be zero or positive (this corresponds to a parabola bending down). This ensures that the emission approaches 0 in the high-energy limit.

Figure 1 shows an example of the observed count spectrum, the counts from the best fit model and the normalized residuals for a 4 second interval near peak time of the event of 17-JAN-2005.

3. Spectroscopy Results

Figure 2 shows lightcurves of the photon spectral index γ and the flux normalization F_{50} (as given in Eq. 1) for the events of Table 1, as found by the spectral fitting procedure explained in Sect. 2.

The observed spectral variability of flares on time scales down to ten seconds or less makes it important to use the highest possible temporal resolution for the spectral fitting (about 4 seconds in our case). Longer integration times, while desirable for better photon statistics, are not suitable because the averaging effect coming from summing spectra of different hardness blurs the spectral evolution. Nevertheless, during the decay phase the flux is so low that full resolution spectra deliver
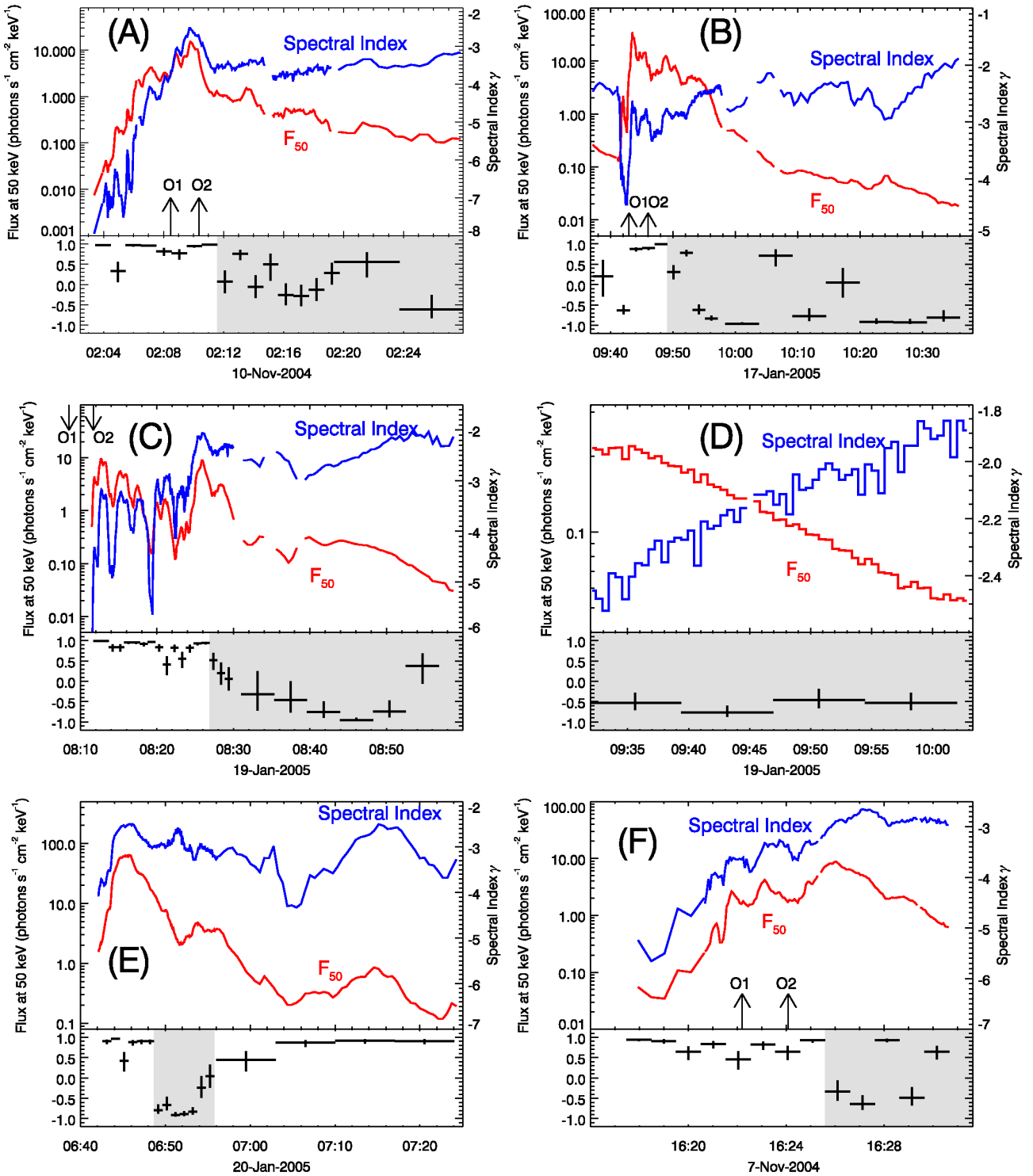
Fig. 2. Temporal evolution of γ and F_{50} for several events. Below each pair of lightcurves a plot of the correlation coefficient between the two curves is shown, as determined during the time intervals indicated by the horizontal bars. The vertical bars represent the 68% confidence level interval. The onset times of the flare associated CMEs are marked as arrows, where O1 and O2 indicating, respectively, linear and quadratic extrapolations.

noisy values for the fitting parameters. In this case, longer integration times must be used. This is acceptable, since during the decay phase the variations of the hard X-ray flux are slower, and short-lived spikes are less frequent. Therefore, some parts of the light curves shown in Fig. 2 have the lower cadence of approximatively 32 seconds (that is 8 RHESSI rotations) in the decay phase.
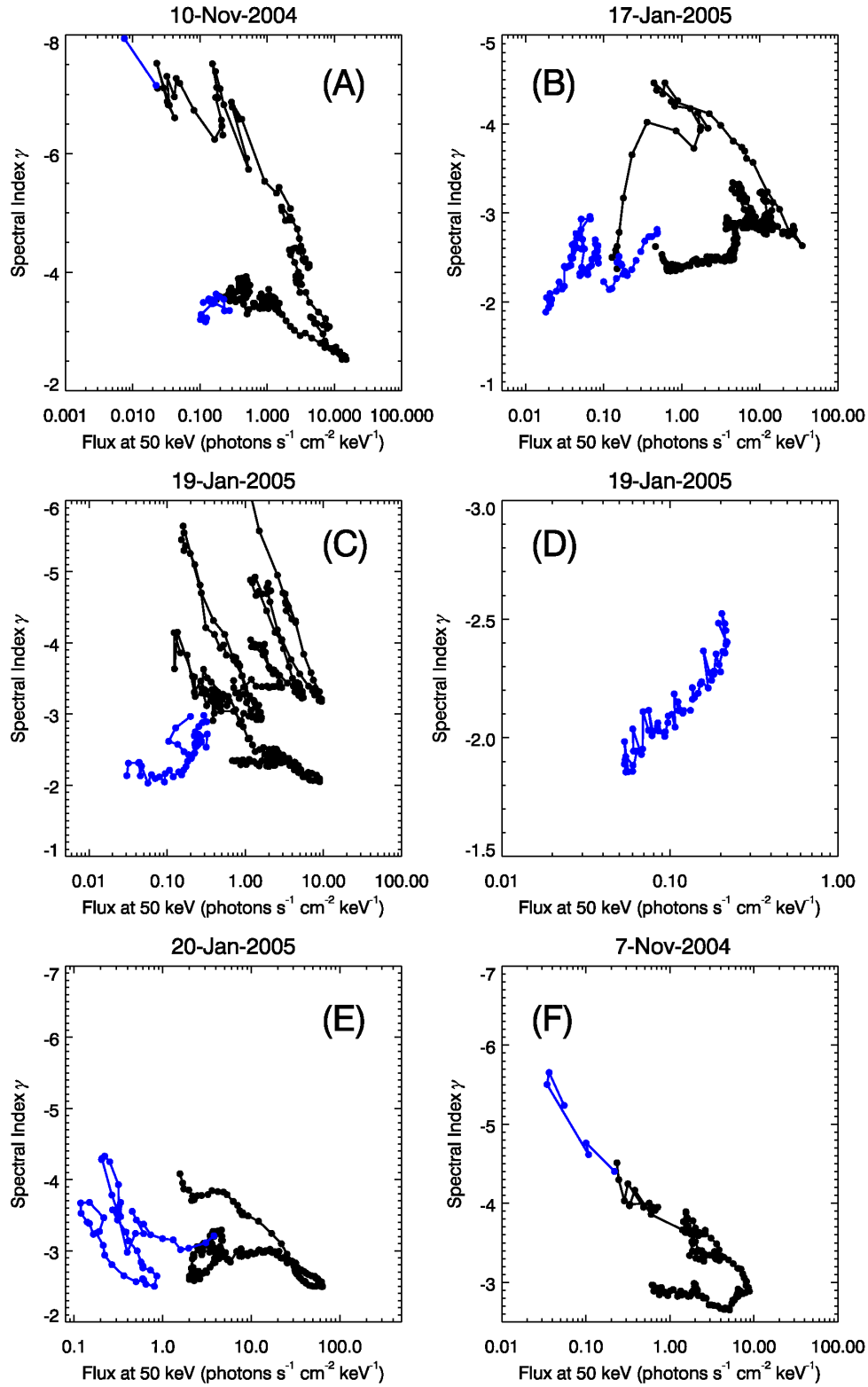
Fig. 3. Spectral index γ vs. flux F_{50}.

Short gaps lasting about 1 minute can be seen in the lightcurves: they corresponds to periods where the thick attenuator was removed from the field of view, but the X-ray flux was still so large that the deadtime in the detector prevents meaningful spectral analysis.

The selected flares show the presence of many distinct emission spikes. SHS peaks are characterized by a correlation in time of γ and $\log F_{50}$, yielding roughly parallel curves. On the other hand, in the presence of SHH peaks or progressive hardenings, the two lightcurves diverge. This is exemplified by
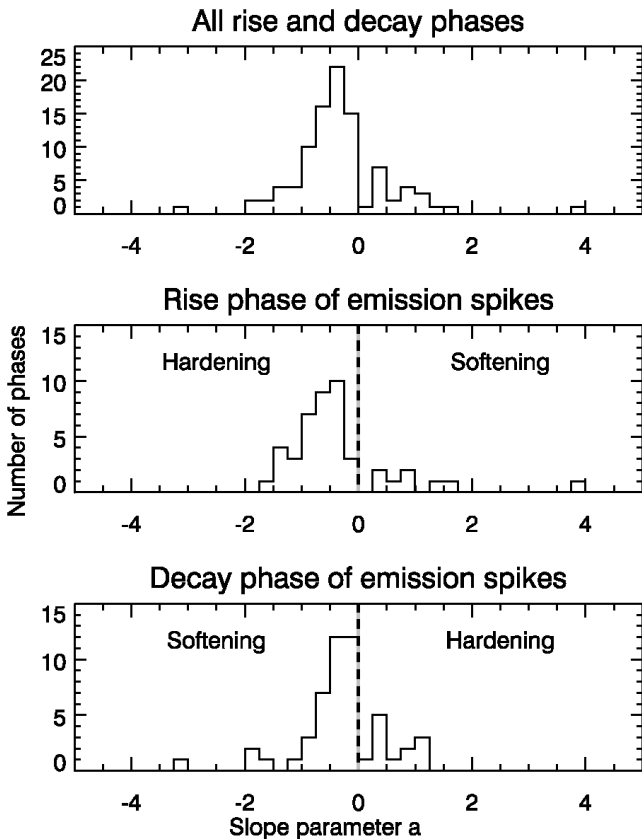
Fig. 4. Distribution of the slopes (parameter a in Eq. 3) for all rise and decay phases of the observed events (upper panel) and for rise and decay phases separately (middle and bottom panel, respectively).

the event of 19-JAN-2005 (Fig. 2, panel C), where the two lightcurves run roughly parallel until 08:29 and then start to diverge.

To better distinguish between the SHS and the hardening trends, Fig. 2 also shows the correlation coefficients between the spectral index γ and the logarithm of the flux $\log F_{50}$ as a function of time. The vertical bars represent the 68% confidence level interval. SHS peaks are characterized by a correlation coefficient close to +1, whereas times where the spectrum hardens while the flux becomes lower have a negative value of the correlation coefficients. We note that during the times when SHS is present there is a strong correlation (near +1), whereas the hardening phases are more erratic and the correlation coefficients is not necessarily close to -1. This shows that for the periods of hardening it may in general not be possible to find a behavior similarly well-defined as it is found for the SHS peaks. In some cases (19-JAN-2005, 08:28 to 08:30), the spectral hardness stays nearly constant while the flux decays. This yields a correlation coefficient near zero.

It should be noted here that most periods showing hardening are weak in flux, and therefore the corresponding lightcurves may be noisy, weakening the correlation. Special care has to be taken in interpreting this curves, as periods near maxima and minima of the curves also deliver lower correla-

tion coefficients if the time interval over which the correlation is computed is comparable with the length of the flat period.

During the late phase of the event of 19-JAN-2005, in the RHESSI orbit following the one featuring the main peak, an uninterrupted phase of hardening is seen from 09:35 to 10:00 while the flux decays exponentially (see Fig. 2, panel D). After that time, the emission reaches a hardness comparable with the one of the background, and it becomes impossible to disentangle the two components by purely spectral methods. This event will be investigated in more detail in Section 5.

We also compared the start of the hardening with the onset time of flare-associated CMEs, taken from the SOHO LASCO CME catalog (Yashiro et al. 2004). In three cases (panel A, B and F) the onset of the CME precedes the start of the hardening by 3 to 5 minutes, in one case by 15–20 minutes (panel C) and in one case by 50 minutes (panel E). In all the events observed an associated CME was present, but the hardening phase never starts before the CME onset.

Figure 3 shows the relationship between γ and $\log F_{50}$. Since the flux increases from left to right and the hardness increases from top to bottom, SHS peaks are expected to show up in the plots as piecewise linear trends with a negative slope (Grigis & Benz 2004, 2005a), while progressive hardening during flux decay times should be visible as a trend with positive slope. Such a relation can be written as

$$\gamma = -a \log(F_{E_0}) + b, \tag{2}$$

where $a < 0$ for the SHS peaks and $a > 0$ during hardening phases (the minus sign in front of a takes care of the fact that in Figs. 2 & 3 the vertical axis for the spectral index is reversed).

Careful examination of the plots in Fig. 2 and 3 reveals that

– Most of the emission spikes are well represented by straight lines in the rise and decay phase. The decay phases are sometimes flatter than the corresponding rise phases (e.g. panel C), but the opposite is also observed (panel A). The event shown in panel E shows some significant deviations from the piecewise straight trend.
– Spectral variability is stronger at the beginning of the event (panels A, B, C, F).
– In the late phase of the events a slower varying component is seen, piecewise straight, mostly nearly flat, slowly hardening (panels B, D), slowly softening (panels A, F), staying at an approximate constant hardness (panel C), or a mixture of the above (panel E).
– During the rise phase up to the strongest peak, the hardness tends to increase from peak to peak (panels A, C). Events are softer at the beginning (all panels).

The piecewise linear trend with negative slope in SHS peaks can be geometrically interpreted as a fixed intersection point of the power-laws at different times, the *pivot point* (Grigis & Benz 2005a), located below the reference energy E_0. Similarly, piecewise linear trends with positive slope can be interpreted here as pivot points at energies larger than E_0 (since we are fitting a log-parabolic model, it is the tangents to the spectrum at E_0 in log-log space that are intersecting, rather than the curves themselves).

The description in terms of a pivot point has the advantage that it does not depend on the choice of the reference energy E_0. On the other hand, the pivot point energy jumps from 0 to $+\infty$ when the slope in γ-$\log F_{E_0}$ space goes from negative to positive. The relation between the pivot point coordinates E_*, F_* and the line parameter a, b in Eq. 2 is given by

$$a = \frac{1}{\log(E_*/E_0)} \qquad b = \frac{-\log F_*}{\log(E_*/E_0)}. \qquad (3)$$

Figure 4 show the distribution of the value of the slope (parameter a in Eqs. 2 and 3) over different rise and decay phases of the emission spikes seen during the 5 events. During a rise phase, a negative slope represents a hardening and a positive slope a softening. The opposite happens during a decay phase. SHS peaks have $a < 0$ both in the rise and decay phase.

The histograms for the rise and decay phase are slightly different: hardenings during rise have a steeper trend than softenings during decays. More precisely, the average value of a when restricted only to negative values is of -0.70 ± 0.06 (the uncertainty is the standard error of the mean) during the rise phases and -0.51 ± 0.08 during the decay phases (after removing the outlier with slope -3.2), a marginal difference. The average of a for the combined set of rise and decays is -0.60 ± 0.05, corresponding to an average pivot point energy of $E_* = 9.4 \pm 1.3$ in agreement with Grigis & Benz (2004).

Examination of the hardenings during decay and softenings during rise phases, restricted to the range 0–3, delivers for the average of a the values 0.66 ± 0.11 and 0.88 ± 0.18, respectively. These values are not significantly different frome each other or from the corresponding absolute value of the $a < 0$ averages.

4. Imaging results

We have investigated whether there is a connection between the spectral evolution and the position of the hard X-ray footpoint sources. To this end, we produced CLEAN images, using detectors 3 to 8, with a cadence of 60 seconds. In particular, we looked for differences in the source positions and speeds during the periods showing hardening.

The event of 19-JAN-2005 was particularly interesting, as it was well observed and the footpoints (FP) clearly move along the ribbons noticeable in a TRACE image at 1600 Å. The motion is fast at the beginning and slows down afterwards. The thermal source is in the form of a loop, and rises throughout the event. This is in agreement with the standard two-dimensional reconnection model for solar flares.

Figure 5 shows the displacement of the northern FP source in two directions, parallel and perpendicular to the ribbon. During the SHS phase, the FP starts moving at around 50 km s^{-1} and slows down continuously until the start of the hardening phase, where it becomes nearly stationary. However, there is no evidence of an abrupt transition between the two regimes.

This is the only event clearly showing this trend (footpoints drifting apart and coming to a stop at the time the hardening starts). The other events show different behaviors.

In the following we report a short description of the morphological behavior of the sources and their evolution for all the events. We distinguish between footpoint sources and
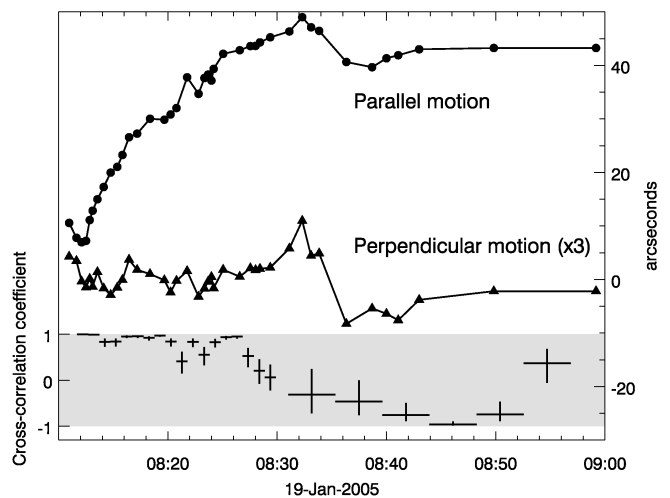

Fig. 5. Movement of the northern footpoint source for the event of 19-JAN-2006. The upper curves show the motion in the two components parallel (top curve) and perpendicular (bottom curve, multiplied by a factor of 3) to the ribbon. The shaded area contains the cross correlation coefficients between hard X-ray spectral index and flux, showing the start of the hardening trend around 08:27.

coronal sources. Because of projection effects, we cannot always infer the real three dimensional structure of the sources, however we know from limb event observations (Battaglia & Benz 2006) that FP sources are mainly nonthermal and well-observed above 20-30 keV, whereas coronal sources are mainly thermal and well-observed below 20-30 keV. Therefore, in the following, we call the thermal source coronal, and the nonthermal sources footpoints.

07-NOV-2004: This events features two footpoints and a coronal source. The eastern FP moves from W to E from 1620 to 1624, jumps back near the starting position and moves again from W to E from 1625 to 1630. The western FP moves slightly from SW to NE from 1621 to 1624, then changes direction, with a slight jump to W and slowly moves to NW from 1625 to 1630. The western FP is brighter than the eastern FP before 1624 and dimmer after 1625. The thermal source is located farther E than the FPs and moves slightly to N from 1619 to 1625, and is not clearly seen in the images afterwards, due to the interposition of RHESSI's thick attenuators.

The jump in position around 1625 roughly coincides with the time at which the hardening starts, possibly indicating that another loop is actively accelerating electrons, but the expansion of the loop, as usggested by the FP motions, continues during the hardening phase, contrarily to what has been observed in the event of 19-JAN-2005.

10-NOV-2004: This event has a very complicated FP morphology, with sources and source-pairs appearing in many different places. It is not possible to find a well-defined source motion like in the simpler cases with only two footpoints. Here the sources seem to jump around as new footpoints in a different position become brighter and outshine the old ones.

Table 2. Source motion near the onset of hardening.

Event	Onset of hardening	Footpoints motion	Coronal source motion
07-NOV-2004	16:26	Jump in the position of the eastern FP	uncertain (bad images at
		Change in the direction of motion of the western FP	low energies after onset)
10-NOV-2004	02:12	Jump in the position of the two brighter FPs	stationary
17-JAN-2005	09:49	Nearly continuous motion of both FPs	continuous motion
19-JAN-2005	08:27	Continuous motion of the northern FP, slowing after the onset	continuous motion upward
		Nearly stationary position of the southern FP	
20-JAN-2005	06:49	Reversal in the direction of motion of both FPs, slowing down afterwards	continuous motion upward

Important shifts in position occur at 0208 and 0212. The latter shift happens at the same time than the onset of hardening.

17-JAN-2005: Three pairs of FPs are seen. The northern pair is stationary and seen from 0943 to 0945. The southern pair consists of an eastern FP moving to SE from 0945 to 1005, and a western FP moving to N from 0943 to 0947, then shifting to W (0955) and moving very slowly to N until 1005. The last pair of FP is to the east and stationary from 1011 to 1029. Coronal sources are seen in two locations: one to the N of the southern FP pair, moving to N from 0946 to 0957, and the second to the NW of the easternmost FP pair, nearly stationary from 1016 to 1030.

There is no clear signature of a discontinuity or a change of behavior happening around 0950, when the hardening starts.

19-JAN-2005: two footpoint are seen with a loop-shaped coronal source between them. The northern FP moves to NE from 0812 to 0830 (covering nearly 60 arcseconds) while the southern FP moves, slower, to SE. In the meantime the loop-shaped coronal source moves to NW (indicating that it is likely rising). After 0830 (only 3 minutes after the onset of hardening) the northern FP is much slower. The coronal source keeps moving to NNW. In the next RHESSI orbit (after 0930), the FP sources can still be seen near the old positions at 0830. The northern FP is nearly stationary from 0933 to 0959, while the southern FP very slightly moves to W, and the coronal source slightly moves to N.

20-JAN-2005: this near-limb event features two FPs and a loop-like coronal source. The southern FP moves to W while the northern FP moves to E. The eastward motion of the northern FP is not continuous: at 0649 it reverses and goes back until 0655, when another sources appears 20″ to E. The double structure lasts until 0701, when the easternmost source fades away. The coronal source moves to NW and rises throughout the event, slowing down towards the end. The reversal coincides with the start of the hardening phase.

The observed behavior at the onset of hardening for all events is reported in Table 2, from the analysis of the source motions in an interval of time spanning 4 minutes, centered on the onset of hardening. We can summarize the imaging observations as follows: there is no universal trend holding for all events. Sometimes, there seems to be a switch to a different loop system near the beginning of the hardening phase. On the other hand, such jumps can also be seen during the SHS phase of the events, so they need not be significant. There is also some indication that the FP motion is slower during the hardening phase, but again this does not hold for all events. In the event of 19-JAN-2005, with a simple geometry and well observed, the change in spectral behavior leading to the hardening phase does not have an impact on the morphology of the hard X-ray sources seen by RHESSI.

5. Modeling

Grigis & Benz (2006) showed that the soft-hard-soft trend is expected from a transit-time damping stochastic acceleration model that includes escape of particles from the accelerator. The hardness is controlled by how fast the particle gain energy in the accelerator and how long they are trapped. Harder spectra result from longer dwelling times of the electrons in the accelerator and higher acceleration efficiency. These conditions also allow a larger population of high-energy electrons to build up, leading to increased hard X-ray emission from the accelerator, identified as a part of the looptop source. Thus the model predicts that harder spectra also have larger hard X-ray flux, but cannot explain the hardenings seen as the flux decays, because it associates harder spectra with larger flux.

The stochastic acceleration model makes a prediction about the spectral evolution of the looptop source. However, the spectroscopy results presented here are obtained by whole-disk spectroscopy, and are therefore dominated in the non-thermal range by footpoint emission. The footpoint spectrum is different than the looptop spectrum (Battaglia & Benz 2007), can be modified by transport effects and is more sensitive to the energy-dependence of the escape term in the acceleration porcess than the looptop source. Therefore, a thorough understanding of footpoint spectra requires more accurate physical modeling of the various processes of acceleration, escape and transport, going beyond the scope of this work.

There is however at least one simple scenario which could lead to hardening trends *in the footpoints* if the electrons in the accelerator are trapped below a certain threshold energy E_T, then the photon spectra will harden below E_T, since the emitting electron population has a low-energy cutoff at E_T. Therefore, if E_T increases with time, the photon spectrum below E_T gets harder and harder, while the flux decreases. This is shown in Fig. 6, where photon spectra computed from electron distribution with the same spectral index and increasing low-energy cutoff energies are shown. We see that the photon
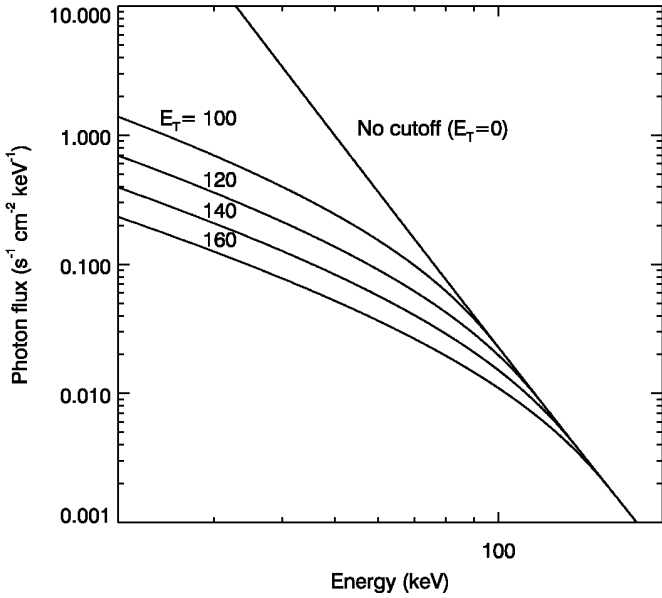
Fig. 6. Photon spectra from thick target emission from electron distributions with low-energy cutoffs E_T of, from the top to the bottom curve respectively, 0, 100, 120, 140, 160 keV. The original electron distribution has a spectral index of $\delta = -6.5$ above the cutoff.

spectra have a nearly constant but slightly increasing hardness while the flux decreases, a situation similar to the late phase of the event of 19-JAN-2005.

Therefore, we investigate here whether an electron spectrum of constant spectral index and flux normalization can give rise to a hardening effect comparable to the one observed if the low-energy cutoff E_T is increased with time. We do not expect such a simple scenario to reproduce all the details of the spectral evolution, but we try to find out in general terms whether it is compatible with the kind of spectral evolution we observe in the decay phase of the events.

An energy distribution of fast electrons in a plasma with a sudden increase is known to be unstable, therefore our scenario also includes an alternative electron distribution featuring a turnover at E_T, that is, a flat distribution below E_T, instead than a cutoff. The electron distributions with cutoff and turnover are given by, respectively,

$$N_{\text{CUTOFF}}(E) = \begin{cases} \Phi_{E_0} \left(\dfrac{E}{E_0} \right)^{\delta} & \text{if } E \geq E_T \\ 0 & \text{if } E < E_T \end{cases} \qquad (4)$$

$$N_{\text{TURNOVER}}(E) = \begin{cases} \Phi_{E_0} \left(\dfrac{E}{E_0} \right)^{\delta} & \text{if } E \geq E_T \\ \Phi_{E_0} \left(\dfrac{E_T}{E_0} \right)^{\delta} & \text{if } E < E_T \end{cases} \qquad (5)$$

The free parameters are the electron spectral index δ, the electron flux normalization Φ_{E_0} (electrons s^{-1} keV^{-1}), the cutoff or turnover energy E_T. The reference energy E_0 is fixed at 50 keV.

To compare the turnover or cutoff model with the observations, we need to find the values of the photon spec-
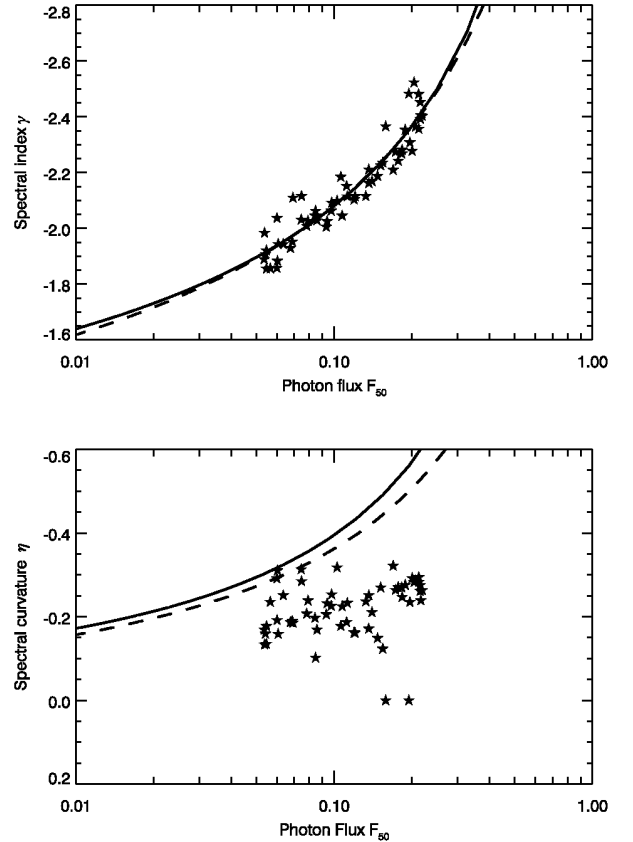

Fig. 7. Observed values of γ vs. F_{50} (*top panel*) and η vs. F_{50} (*bottom panel*), represented as stars, with the model curve (continuous for the cutoff model, dashed for the turnover model) expected from a constant electron hardness and flux, but rising low energy cutoff or turnover energy E_T.

tral parameters γ, η and F_{50} resulting from the emission of an injected electron distribution $N_{\text{CUTOFF}}(E; \Phi_{50}, \delta, E_T)$ or $N_{\text{TURNOVER}}(E; \Phi_{50}, \delta, E_T)$ impacting on a thick target.

This is done by computing the thick target emission by the electron spectra, assuming collisional energy losses and using the full relativistic Bethe-Heitler cross section (Bethe & Heitler 1934) for bremsstrahlung emission with the Elwert (1939) correction factor. This generates a model photon spectrum. To ensure a fair comparison with the observations, we fit a logarithmic parabolic model in the energy range 20-80 keV to the model photon spectra, in the same way as was done for the observational data (but without having to deal with the instrumental response matrix and the background issues). Thus we can directly compare the parameters γ, η and F_{50} from the observations and from the cutoff or turnover model.

For fixed values of δ and Φ_{50}, a change in E_T generates the curves $F_{50}(E_T)$ and $\gamma(E_T)$. We can then fit the values of δ and Φ_{50} such that the observed values of F_{50} and γ lie as close as possible to the curves.

The late phase of the event of 19-JAN-2005, from 09:32 to 10:02, consists of 30 minutes of continuous hardening, and therefore is well suited for the comparison with the simple cutoff or turnover model. Figure 7 show the comparison, where

the observed values of γ and η are plotted as a function of F_{50} together with the best-fit model curve for both the cutoff and turnover electron spectra. For the cutoff model, the best fit values of the parameters are: spectral index $\delta = 6.52$, flux normalization at 50 keV $\Phi_{50} = 4.50 \cdot 10^{33}$ electrons s^{-1} keV^{-1} while E_T is increased from 98 to 159 keV (thus yielding a photon spectral index γ in the range between -2.5 and -1.9). The corresponding values for the turnover model are: $\delta = 6.11$, $\Phi_{50} = 3.67 \cdot 10^{33}$ electrons s^{-1} keV^{-1}, while E_T is increased from 127 to 224 keV.

The photon spectra from both the cutoff and turnover model are strongly curved downward in the fitted energy range. The spectral curvature η is observed to be between 0 and -0.3, whereas the model spectra have values around -0.55 to -0.25.

The total fluxes of electrons in the injected spectrum are of $9.9 \cdot 10^{32}$ electrons s^{-1} for $E_T = 98$ keV and $6.6 \cdot 10^{31}$ electrons s^{-1} for $E_T = 159$ keV, and the total injected powers are, respectively, $1.9 \cdot 10^{26}$ erg s^{-1} and $2.1 \cdot 10^{25}$ erg s^{-1}. The total number of particles for the turnover model when E_T is increased from 127 to 224 keV goes from $2.3 \cdot 10^{33}$ to $1.3 \cdot 10^{32}$, and the energy (power) from $1.9 \cdot 10^{26}$ erg to $2.8 \cdot 10^{25}$ erg.

Moreover, if particle trapping really is so efficient, than an accumulation of electron below the threshold energy E_T is expected, which should be visible as a high-energy coronal source. This is not observed, as the 25-50 keV images are clearly dominated by footpoint emission.

This simple scenario is able to reproduce the observed features of the hardening observed, but fails to yield the correct spectral curvature. The curvature is however a second-order parameter and therefore its measurements by spectral fitting is harder, as can be seen by the larger dispersion in the bottom plot of figure 7, but the difference between prediction and observations is large enough to be real.

6. Discussion

Spectroscopic RHESSI observations with a 4 second cadence are well suited to study the spectral evolution during the main phase of large flares, while the early rise and late decay phases need longer integration times to allow meaningful spectral fitting. Due to the large amount of data involved (more than 3 thousand spectra) it was necessary to have an automated fitting routine. For every spectrum, 2 preliminary passes were done estimating the parameters for the thermal and the non-thermal part which were then used as starting parameters for the final fitting. This turned out to deliver good fittings for most of the data. A check of the quality of the data was performed by looking at the time evolution of χ^2 and of the fitting parameters. Spectra with reduced χ^2 worse than 2 were manually fitted again, and in most cases it was possible to find another set of fit parameters yielding reduced χ^2 below 2, with the exception of the event of 20-JAN-2005.

This event (the largest flare, GOES class X7) is characterized by very strong thermal emission. At times when the nonthermal emission is weak and/or soft, pileup effects are especially large in the 20-50 keV band. Therefore, the fittings, which are good above 50 keV, have large residuals below that energy. This may be due to the fact that the photon spectrum model chosen is not suited to describe the observed photon spectra, or that the pileup correction is inaccurate. Because it is very hard to correctly take into account pileup effects in such a regime, it is not clear whether the model failure is real or instrumental. Therefore, we let the spectrum model stand as it is, but caution that the fitting parameters for the flare of 20-JAN-2005 may be less accurate than in the other events, due to the unknown systematic effects generated by imperfect pileup correction.

For the other events, the fit parameters are of good quality and the corresponding photon models are a high-fidelity representation of the incoming photon flux. The final distribution of the reduced χ^2 for all events (except 20-JAN-2007) is such that 89% of all spectra have χ^2 less than 1.5 and 97% of all spectra have χ^2 less than 2. Therefore the unusual choice of the logarithmic parabolic fit-model, explained in Sect. 2, produces good fittings and is therefore justified *a posteriori*.

The path observed in the γ vs. log F_{50} plots for the events is not simple. However, it can be broken down reasonably into a superposition of linear trends during flux rise and decay phases. While not all rise or decay phases can be so decomposed, this simple description is adequate for most of them, and permits observational and theoretical comparison.

There is a difference between the results reported here and the results from Grigis & Benz (2004) in the asymmetry between rise and decay phases in SHS peak. The previous results indicated that decay phases are steeper in the γ vs. log F_{50} plot than rise phases, were here we find the opposite. The reason probably is the selection bias: here we looked specifically for events showing hardening. This hardening trend sometimes overlays SHS peaks, giving rise to a soft-hard-less-soft pattern.

The hard X-ray images during the events show the usual morphology of hard X-ray solar flares: a low-energy coronal source and two or more high-energy footpoint sources. The position of the footpoint sources is strongly variable: they are observed to either smoothly move around or jump from location to location. This reflects changes in the connection between the accelerator and the chromosphere, as well as in the location of the accelerator itself.

The behavior observed in the images cannot be reconduced to one simple scenario valid for all events. However, the observations seem to point out that there is no clear separation between the SHS and the hardening phases: the former seems to smoothly merge into the latter. Even in the cases where the emission jumps at the onset of hardening (Table 2), the footpoint behavior there seems not to be radically different.

The scenario presented in Sect. 5 is quite simple, but allow us to focus on one of the key issues raised by the observations: is the accelerator still working during the late, hardening phase? The alternative option would be that high-energetic electron are trapped in the corona and are slowly released and injected in the chromosphere. Noting that this hardening phase lasts about 30 minutes and that the decay of the flux in time is nearly exponential (as seen by the fact that the F_{50} line in Fig. 2, panel D, is nearly straight), we can compute the total number

of injected electrons from the total electron fluxes at the start F_{BEG} and at the end F_{END} by using

$$F_{TOT} = \Delta t \frac{F_{END} - F_{BEG}}{\log \dfrac{F_{END}}{F_{BEG}}} , \qquad (6)$$

where Δt is the observation interval length (here 30 minutes) and F_{TOT} the total injected flux. From the observed values, we get $F_{TOT} \simeq 1 \cdot 10^{36}$ electrons for the turnover model and $F_{TOT} \simeq 6 \cdot 10^{35}$ electrons for the cutoff model. These numbers do not seem extraordinarily high, but it should be noted that all these electron have energies above 100 keV.

Such a large population of electrons would be seen as a strong coronal hard X-ray source in the 50 - 100 keV band. The luminosity depends on the volume and density of the region where they are stored, but it would be visible on RHESSI images unless it were a very large low-density loop. The observed footpoints in the hardening phase are separated from each other by approximatively $60''$, indicating a large but not huge loop.

Both the cutoff and turnover model are able to reproduce the observed γ vs. $\log F_{50}$ trend, but fails to reproduce the correct spectral curvature η. Although the observation of η is more difficult in the decay phase due to the lower signal-to-background ratio, the difference between the cutoff and turnover models and the observed points is significant. The value of the parameter η depends on the energy interval chosen for the fitting of the model photon spectra (20-80 keV in our case). A lower maximum energy of this interval produces lower model values for η.

We note here that if the accelerator is inhomogeneous, and the electron spectrum at the footpoints is the superposition of different components with different values of the low-energy cutoff or turnover E_T, this could lead to a reduction of the observed spectral curvature down to the observed values.

7. Conclusions

Here, we tie together the results of spectroscopy, imaging and the simple modeling presented in this paper. The main results of the analysis of the large events studied are:

– The flares selected show both the soft-hard-soft behavior and the presence of hardening trends. The hardening starts at or after the largest peak of the flares. In 3 out of 5 events it starts 2 to 6 minutes after the onset of a CME.
– Similar to SHS peaks, hardening phases can usually be described by piecewise linear trends in a plot of spectral index vs. logarithmic flux.
– There is no clear trend relating the behavior of footpoint sources with the spectral evolution holding for all events. Sometimes the location of the emission shifts when the hardening starts, in other events it does not.
– In the event of 19-JAN-2005, where there are only two well-defined footpoint sources over the whole events which can be tracked, there is no discontinuity in the position at the onset of hardening, but a general trend of slowing down, such that the FP is nearly stationary during the decay phase.

– In 3 out of 5 flares, the coronal source was moving continuously during the onset of the hardening. This motion was probably directed upwards in two near-limb events.

These results support the view that the acceleration mechanism gradually changes in the later phase of the flare, having clear effects on the spectrum, but a more indirect and subtle influence on the source position.

In the sample studied we find a surprising lack of detailed correlation between the spectral and spatial behavior, similar to what has been observed by Grigis & Benz (2005b) in a slightly smaller flare (M6) featuring strong footpoint motions and hardening at the end.

The main question addressed in this paper is whether the SHS peaks and hardening phases are the results of two different acceleration mechanisms. While the data gathered here cannot give a final answer to this question, we have discovered strong evidence pointing out that there is a gradual change in the accelerator itself, transforming its behavior from impulsive (showing up as SHS peaks) to gradual (hardening phases). This is substantiated by the observations of the superimposition of SHS peaks with a continuous hardening trend and of the smooth footpoint motions during the onset of hardening.

As the footpoints drift apart, acceleration takes place in larger and larger loops. In a stochastic acceleration framework, the acceleration efficiency of electrons in larger loops is reduced, while ions can be more efficiently accelerated (Emslie et al. 2004). Since hardening trends are well correlated with the occurrence of interplanetary energetic protons events, it is possible that the very conditions that are responsible for the hardening trends favor acceleration of protons, which may then escape into interplanetary space, with the CME controlling their release rather than acceleration (Simnett 2006).

Different coronal loops may be involved in particle acceleration during a flare, with different physical properties as of their size, density, magnetic field, etc. The overall magnetic geometry of the active region will determine which loops reconnect at which time, sometimes giving rise to an orderly motion of footpoints, sometimes generating a more chaotic situation. The data suggest that as the reconnection process proceeds, some physical parameters of the accelerator changes in such a way as to favor the production of harder spectra, rather than having a totally new process (say, shock acceleration) taking over in the decay phase.

References

Battaglia, M., & Benz, A. O. 2007, A&A, 466, 713
Battaglia, M & Benz, A. O. 2006, A&A, 456, 751

Battaglia, M., Grigis, P. C., & Benz, A. O. 2005, A&A, 439, 737

Bethe, H., & Heitler, W. 1934, Royal Society of London Proceedings Series A, 146, 83

Cliver, E. W., Dennis, B. R., Kiplinger, A. L., et al. 1986, ApJ, 305, 920

Dulk, G. A., Kiplinger, A. L., & Winglee, R. M. 1992, ApJ, 389, 756

Frost, K. J., & Dennis, B. R. 1971, ApJ, 165, 655

Emslie, A. G., Miller, J. A., & Brown, J. C. 2004, ApJ, 602, L69

Elwert, G. 1939, Ann. Phys. 34, 178

Grigis, P. C. & Benz, A. O. 2004, A&A, 426, 1093

Grigis, P. C., & Benz, A. O. 2005a, A&A, 434, 1173

Grigis, P. C., & Benz, A. O. 2005b, ApJ, 625, L143

Grigis, P. C., & Benz, A. O. 2006, A&A, 458, 641

Hudson, H. S., Lin, R. P., & Stewart, R. T. 1982, Sol. Phys., 75, 245

Kahler, S. W. 1984, Sol. Phys., 90, 133

Kiplinger, A. L. 1995, ApJ, 453, 973

Lin, R. P., Dennis, B. R., Hurford, G. J., et al. 2002, Sol. Phys., 210, 3

Massaro, E., Cusumano, G., Litterio, M., & Mineo, T. 2000, A&A, 361, 695

Ohki, K., Takakura, T., Tsuneta, S., & Nitta, N. 1983, Sol. Phys., 86, 301

Parks, G. K., & Winckler, J. R. 1969, ApJ, 155, L117

Simnett, G. M. 2006, A&A, 445, 715

Takakura, T., Sakurai, T., Ohki, K., Wang, J. L., Zhao, R. Y., Xuan, J. Y., & Li, S. C. 1984, Sol. Phys., 94, 359

Wild, J. P., Smerd, S. F., & Weiss, A. A. 1963, ARA&A, 1, 291

Yashiro, S., Gopalswamy, N., Michalek, G., St. Cyr, O. C., Plunkett, S. P., Rich, N. B., & Howard, R. A. 2004, Journal of Geophysical Research (Space Physics), 109, 7105